





Article

# Rebar Shape Time-Evolution During a Reinforced Concrete Corrosion Test: An Electrochemical Model

Guillem de Vera <sup>1,\*</sup>, Marina Miró <sup>1</sup>, Enrique Gonzalo Segovia <sup>1</sup>, Pedro Poveda <sup>2</sup> and Miguel Ángel Climent <sup>1</sup>

<sup>1</sup> Civil Engineering Department, University of Alicante, P.O. Box 99, 03080 Alicante, Spain

<sup>2</sup> Department of Physics, Systems Engineering, and Signal Theory, University of Alicante, P.O. Box 99, 03080 Alicante, Spain

\* Correspondence: guillem.vera@ua.es

Received: 27 June 2019; Accepted: 24 July 2019; Published: 29 July 2019



**Abstract:** An electrochemical model is presented to calculate the rebar shape time-evolution in reinforced mortar specimens during forced corrosion tests. This provides a more realistic description than the usually used geometric models. The current distribution along the rebar perimeter is calculated by using Finite Element Method (FEM) to solve Laplace equation. Then, Faraday's law is used to relate current distribution to rebar volume increase due to corrosion products creation. The shape of the rebar section is obtained as a function of corrosion time.

**Keywords:** electrochemical model; finite elements; corrosion test; rebar corrosion

## 1. Introduction

Corrosion of steel is one of the main mechanisms limiting the service life of reinforced and pre-stressed concrete structures, both in buildings and civil infrastructure [1]. The expansive character of the steel corrosion products is at the origin of the damage suffered by concrete [2], whose early symptoms are micro and macro cracking [3,4], which is followed by spalling or delamination of the concrete cover. Further consequences of the corrosion of embedded steel are the following: loss of bond between concrete and steel, loss of steel ductility, and loss of cross-sectional area of steel [5]. These phenomena contribute to reducing the serviceability and load bearing capacity of the structures.

Usually the appearance of cracking is considered as the limit state regarding the durability of concrete structures affected by steel reinforcement corrosion [6,7]. Thus, great effort on cracking the understanding has been done [8–16]. Corrosion products' volume is higher than metal volume, and most of the corrosion products remain as a solid layer around the rebar [2,17]. Thus, corrosion implies a rebar volume increase that causes concrete cracking [2]. Moreover, as metal converts in its corrosion products, the structure's strength weakens due to a metal section loss [5].

Cracking is experimentally studied usually by accelerated corrosion tests [9,12,17–20]. Additionally, mechanical models have been developed to obtain numerical simulations [8,10,11,13–16,21]. A key factor on mechanical modelling is the rebar shape time-evolution, which will determine the applied loads on concrete. Some authors accept a uniform expansion along the rebar perimeter [22,23]. Nevertheless, the corrosion rate can vary along the rebar perimeter depending on the exposure conditions. When corrosion is due to a depassivating agent that ingress into concrete from the environment, the corrosion rate of the outer part of the rebar will be higher. The corrosion rate along the rebar perimeter in a forced corrosion test will depend on the cathode location. This non-uniform corrosion has been observed experimentally [19,20] and has also been modelled [10,11,13–16,21]. Usually, geometrical models are used to describe the rebar section and the rebar shape is considered as an ellipsoid [11,14,15,21], a combination of ellipsoids [18], or other geometries [12,13] depending on

exposure conditions. This is a convenient simplification for a modelling purpose, but a more realistic model would be desirable. Some detailed models [10,11] have been developed for chloride exposure conditions by taking into account chloride transport in order to estimate the non-uniform corrosion along the rebar perimeter. The present paper focuses on a forced corrosion test method, where an electrical current is applied to induce corrosion. An electrochemical model for the estimation of rebar shape time-evolution is presented in order to get a more realistic approach of the rebar shape during the test. This shape could be taken as input for mechanical models trying to simulate concrete cracking due to embedded steel corrosion under these conditions.

## 2. Materials and Methods

Prismatic mortar samples with dimensions 8 cm × 8 cm × 35 cm were fabricated using composition shown in Table 1. Sodium chloride was added to the fresh mix so as to obtain a chloride (Cl<sup>-</sup>) content of 2% relative to cement weight [24]. One 12-mm diameter steel bar was embedded in each sample with a 10-mm mortar cover depth. The ends of the steel bar were protected with vinyl electric tape, which left an exposed steel area of 120 cm<sup>2</sup> (surface of contact steel-mortar). Specimens were cured during seven days in a humid chamber (20 °C and 95% relative humidity). Before starting the forced corrosion test, the spontaneous corrosion rate of the steel bar was measured through the linear polarization technique, using the portable corrosion rate meter Gecor8 (Geocisa, Madrid, Spain).

**Table 1.** Composition of the cement mortar.

Material	Amount (g)
Cement (CEM I 52.5 R SR (3)) [25]	450
Standard siliceous sand	1350
Deionized water	225 (w/c = 0.5)
NaCl	14.8 (2% relative to cement weight)

After curing, the sample was submitted to corrosion galvanostatically, i.e., by applying constant current, for 23 days. The rebar (anode) is connected to the positive pole of a power supply and the negative pole is connected to a galvanized steel mesh (cathode) that is located under the mortar sample. The contact of the cathode with the mortar sample is assured with a wet sponge. The cathode and the lower part of the mortar sample were submerged in tap water to assure good conductivity. A section of the mortar sample is shown in Figure 1 (left). Values of geometric parameters are shown in Table 2. The applied current density is  $j_m^0 = 100 \mu\text{A}/\text{cm}^2$  referred to as the initial rebar surface. Steel mass loss was measured at the end of the corrosion test using the procedure found in Reference [26]. More details of the experimental tests can be found elsewhere [27].

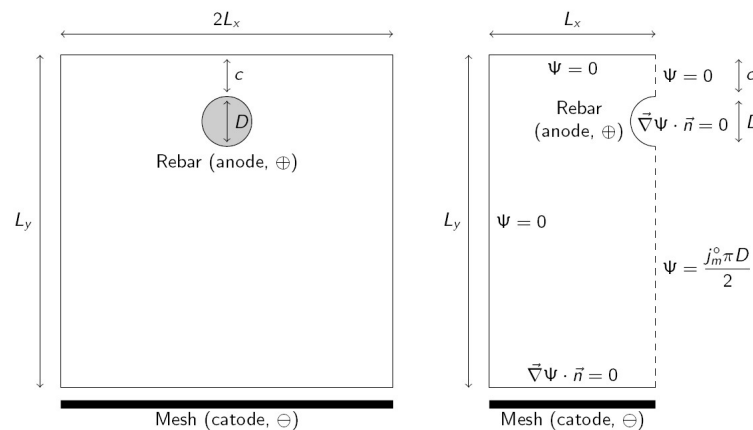


**Figure 1.** Section of the mortar sample in the corrosion test (left) and boundary conditions applied (right, see text for details).

**Table 2.** Parameters used to define mesh and size of the obtained mesh.

Parameters		
$L_x = 4 \text{ cm}$	$L_y = 8 \text{ cm}$	$\Delta t = 0.5 \text{ day}$
$D = 1.2 \text{ cm}$	$c = 1 \text{ cm}$	$\Delta r = 1 \text{ mm}$
$n_x = 30$	$n_y = 60$	$n_b = 50$
Obtained mesh		
Mesh	Nodes	Elements
Initial	1855	3490
After 1 year	1868	3514

### 3. Rebar Shape Model

Rebar metal loss is considered to be due to the anodic impressed current of  $100 \mu\text{A}/\text{cm}^2$ . The measured open circuit corrosion rate, due to the presence of  $\text{Cl}^-$  ions, showed values in the range  $0.7 \mu\text{A}/\text{cm}^2$  to  $3 \mu\text{A}/\text{cm}^2$ . Since this is much lower than the impressed current during the test, it seems suitable neglecting spontaneous corrosion contribution to metal loss in the model. Moreover, theoretical metal loss (evaluated using Faraday's law for a  $100 \mu\text{A}/\text{cm}^2$  current density) is consistent with experimentally observed metal loss. Experimental to the theoretical metal loss ratio mean value was found to be 1.05, with a standard deviation of 0.19 (three samples) [27].

Current density along the rebar perimeter is calculated by solving the appropriate differential equation. The obtained current density is not uniform along the rebar perimeter. Faraday's law is then used to relate current density with the volume of metal lost. Since current density is not uniform, metal loss is also not uniform along the rebar perimeter, and, therefore, the bar loses its initial circular shape. The dissolved metal is assumed to react to form solid corrosion products that are bulkier than the original metal [28]. It is assumed that solid corrosion products stay where they are formed, laying a solid layer of corrosion products around the metallic rebar. The thickness of this layer is also not uniform along the rebar perimeter. As a result, in comparison with the original circular section, a narrower non-circular metal section covered by a non-uniform layer of corrosion products is obtained, which yields, as a whole, a thicker non-circular bar. The bar will become thicker when the current density is higher. This expanded bar will be the cause of mortar cracking.

#### 3.1. Initial Current Density

Current exits from the rebar surface (anode) perpendicular to it and arrives to the mesh (cathode) perpendicular to it. Current density along the rebar perimeter is not uniform. Current density in the lower part of the rebar is higher because it is closer to the cathode. Then, metal loss is faster in the lower part of the rebar. In order to determine the current density distribution along the rebar perimeter, an appropriate differential equation must be solved. The problem is solved in terms of the current function  $\psi$  whose level curves are the current streamlines [19]. Laplace Equation (1) must be solved [29].

$$\frac{\partial^2 \psi}{\partial x^2} + \frac{\partial^2 \psi}{\partial y^2} = 0 \quad (1)$$

Due to the symmetry, Equation (1) can be solved in a half section of the mortar sample, as shown in Figure 1 (right). Boundary conditions are applied as follows (see Figure 1 right). Current flows perpendicular to the rebar surface and then a natural or Neumann boundary condition (null flux of the variable through the boundary) is applied ( $\vec{\nabla} \psi \cdot \vec{n} = 0$ , being  $\vec{n}$  vector normal to the surface). The same boundary condition is applied on the cathode since current also flows perpendicular to it. The symmetry line (dashed line in Figure 1 right) is now considered. Due to symmetry, the current does not traverse this boundary and this implies that essential or a Dirichlet boundary condition (fixed variable value) can be applied, and current function  $\psi$  is constant on the boundary. Nevertheless, the  $\psi$

value will be different above and below the rebar. The value  $\psi = 0$  can be arbitrarily assigned to the upper part of the symmetry line. For the lower part, it is taken into account that the integral of current density along a curve equals the difference in  $\psi$  values between both extremes of the line [29].

$$\psi_b - \psi_a = \int_a^b \vec{j} \cdot d\vec{\ell} \quad (2)$$

Integrating along the rebar perimeter between the top and bottom, and recalling that  $\psi = 0$  at the top, the value  $\psi = j_m^\circ \pi D / 2$  is obtained for the bottom part of the symmetry line. For the remaining boundaries (top and left surfaces of the mortar sample), Dirichlet boundary conditions are applied since current does not flow through them. They are a continuation of the upper part of the symmetry line and then  $\psi$  must have the same value ( $\psi = 0$ ).

A differential Equation (1) is solved using a standard finite elements method [30] and the software Matlab R2013b [31]. The mesh of triangular elements has been constructed as follows. (i)  $n_x \times n_y$  equally spaced nodes are defined in the rectangular domain of size  $L_x \times L_y$ . (ii) Nodes at a distance less or equal to  $\frac{D}{2} + \Delta r$  from rebar center are eliminated, where  $\Delta r$  is a chosen distance. (iii) The rebar boundary is defined with  $n_b$  with equally spaced nodes on the semi-circumference of the radius  $\frac{D}{2}$ . (iv)  $n_b$  equally spaced nodes are added on the semi-circumference of the radius  $\frac{D}{2} + \Delta r$ . This procedure assures more regular elements around the rebar, where a higher precision is required. (v) Mesh is generated with the defined nodes using the Delaunay algorithm (function delaunay from Matlab [32]). (vi) Generated elements that lay inside the rebar are eliminated.

$\psi$  is obtained by solving Equation (1) in the domain. Now, current density along the rebar perimeter must be calculated. In order to do this, the integration curve in Equation (2) is taken along the rebar perimeter from the top to an arbitrary point on the perimeter. The current density on the perimeter is obtained after deriving Equation (2), which yielded the expression below.

$$j(\theta) = \frac{2}{D} \cdot \frac{d\psi}{d\theta} \quad (3)$$

where  $\theta$  is the angle between the rebar top and an arbitrary point on the perimeter of the rebar. Current density will be related to metal loss in Section 3.3. Thus, metal loss will be obtained along the rebar perimeter as a function of angle  $\theta$ .

### 3.2. Current Density Time-Evolution

Current density time-evolution is obtained by solving Equation (1) in small time intervals  $\Delta t$ . The equation to be solved does not change during the test, but boundary conditions will change because the rebar shape changes. After each time step, the rebar shape is recalculated using Faraday's law, which relates current density with metal loss (see Equation (6)). As the rebar shape changes over time, when defining the elements' mesh, it is necessary to replace the initial semi-circumference of radius  $\frac{D}{2}$  that defines the initial rebar by the curve of radius  $r_m(\theta, t)$ , which defines the rebar shape. Thus, the procedure to define the elements' mesh is the same as in the previous section but replacing  $\frac{D}{2}$  by  $r_m(\theta, t)$  in steps (ii), (iii), (iv), and (vi). After solving Equation (1) in each time step, the current density along the rebar perimeter is now calculated as Equation (4) instead of Equation (3).

$$j(\theta, t) = \frac{1}{r_m(\theta, t)} \cdot \frac{\partial \psi(\theta, t)}{\partial \theta} \quad (4)$$

### 3.3. Rebar Shape Time-Evolution

The rebar corrosion causes metal loss and the reduction of the radius of the rebar. The radius loss is not uniform along the rebar perimeter because the current density is not uniform. On the other hand, corrosion products precipitate as oxides that are bulkier than the original metal [2]. In this paper, it is

accepted that these corrosion products remain attached to the bar, giving rise to a metal rebar narrower than the original but covered with a layer of oxides that gives the whole a volume greater than the original. The remaining metal radius  $r_m$  and the radius of the rebar as a whole  $r_{ox}$  (including the oxide layer) are determined in this section. Both depend on the angle  $\theta$  since the current density  $j$  depends on it.

Let  $d\theta$  be a differential rebar angle. The surface subtended by it is  $L_z r_m d\theta$ , where  $L_z$  is the rebar length. The current traversing this surface is  $jL_z r_m d\theta$ , and the circulated charge during an interval  $dt$  is  $jL_z r_m d\theta dt$ . Faraday's constant  $F$  gives the charge of a mole of electrons, then circulated moles of electrons are represented by  $\frac{jL_z r_m}{F} d\theta dt$ . It is related with moles of dissolved metal by the oxidation reaction stoichiometry. Being  $n$ , the moles of electrons needed to dissolve one mole of metal, the moles of dissolved metal during the  $dt$  interval are  $\frac{jL_z r_m}{nF} d\theta dt$ . Using metal molar mass  $M$  and metal density  $\rho$ , the volume of metal lost is  $-\frac{jML_z r_m}{nF\rho} d\theta dt$ . Additionally, this volume can be expressed geometrically as  $L_z r_m d\theta dr_m$ . Equating both expressions, the following is obtained for the metal radius variation.

$$dr_m = -\frac{j(\theta, t)Mdt}{nF\rho} \tag{5}$$

That can be integrated to obtain the metal radius.

$$r_m(\theta, t) = \frac{D}{2} - \frac{M}{nF\rho} \int_0^t j(\theta, t) dt \tag{6}$$

where  $\frac{D}{2}$  is the initial rebar radius. The oxidation reaction considered is shown below [2].



For which  $n = 2$ . The used values of the other constants are  $M = 55.85 \text{ g/mol}$ ,  $F = 96,485 \text{ C/mol}$ , and  $\rho = 7.85 \text{ g/cm}^3$  [33].

The length of the metal perimeter through which corrosion takes place does not remain constant and can be calculated as:

$$s(\theta, t) = \int_0^\theta r_m(\theta, t) d\theta \tag{8}$$

Radius of the rebar as a whole, including the oxide layer,  $r_{ox}$ , is now obtained. Let  $d\theta$  be a differential rebar angle, where the variation of radii during an interval  $dt$  is  $dr_m$  for the metal and  $dr_{ox}$  for the whole rebar including the oxide layer. Then, the variation of metal volume  $dV_m$  and variation of the oxide layer volume  $dV_{ox}$  are geometrically given by:

$$\begin{aligned} dV_m &= L_z r_m d\theta dr_m \\ dV_{ox} &= L_z r_{ox} d\theta dr_{ox} - L_z r_m d\theta dr_m \end{aligned} \tag{9}$$

The volume occupied by the oxides is considered to be  $\alpha$  times the volume occupied by the original metal. The value  $\alpha = 2$  [28] has been considered. Then:

$$dV_{ox} = -\alpha dV_m \tag{10}$$

Using Equation (9) in this case and integrating, the radius of the rebar including the oxide layer  $r_{ox}$  is obtained using the formula below.

$$r_{ox}(\theta, t) = \sqrt{\frac{D^2}{4} - (\alpha - 1)\left(\frac{D^2}{4} - r_m^2(\theta, t)\right)} \tag{11}$$

This radius gives the shape of the rebar that could be used in mortar cracking mechanical models.

#### 4. Results

The parameters used for elements mesh definition are shown in Table 2, where the size of the obtained mesh is also shown. The initial mesh is shown in Figure 2 (left) and a detail of the mesh obtained after one year of corrosion is shown in Figure 2 (right), where the solid line shows the initial rebar shape. In this case, a metal section reduction and a shape change can be seen. The radius decrease is higher on the bottom. This is the expected behavior because the bottom part is closer to the cathode.

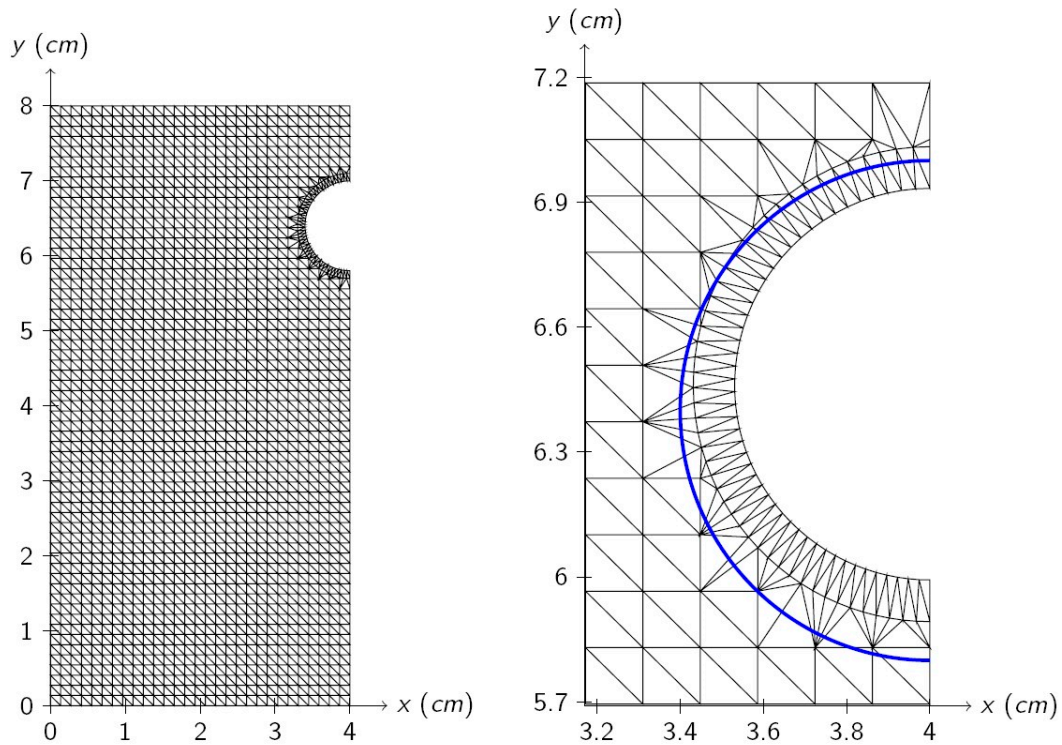


**Figure 2.** Initial mesh (left) and a detail of the mesh after one year of corrosion (right). The blue line shows the initial rebar shape.

Level curves of  $\psi$  (20 of them are shown), i.e., current streamlines, are shown in Figure 3 for the beginning of the corrosion test (left) and after one year of corrosion (right). The dashed line shows the oxide layer. The upper part of the rebar is farther from the cathode, and a higher ohmic drop is expected, which causes a lower current density. This is confirmed by the model, which shows a higher density of current streamlines on the lower part of the rebar. It can also be seen in Figure 3 that the shape of the streamline does not change a lot during time. Nevertheless, the reduction of the metal section implies that the current streamlines are closer on the metal perimeter, which indicates a higher current density on the corroding surface.

The current density on the rebar perimeter is shown as a function of the length of the perimeter of the metal  $s$  in Figure 4 for 0 days (initial), 23 days (duration of the test), and one year. Note that the curves shorten with time because the perimeter of the metal decreases, according to Equation (8). This is accompanied by a current density increase. This is expected because the experiment is carried out galvanostatically i.e., with constant current. Then a surface reduction implies a current density increase. The maximum current density occurs on the rebar bottom ( $\theta = 180^\circ$ , nearest to the cathode) and the minimum on the rebar top ( $\theta = 0^\circ$ , farthest from the cathode). Experimentally, it is observed that the first cracks appears on the sample surface at four days, when current distribution is very similar to the initial [27]. Calculated current density on the rebar bottom and the rebar top when the first cracks occur are, respectively,  $154.13 \mu\text{A}/\text{cm}^2$  and  $46.14 \mu\text{A}/\text{cm}^2$ . It is worth noting that, due to

the reinforced mortar specimen geometry, cracks appear first on the side where the current density is lower.

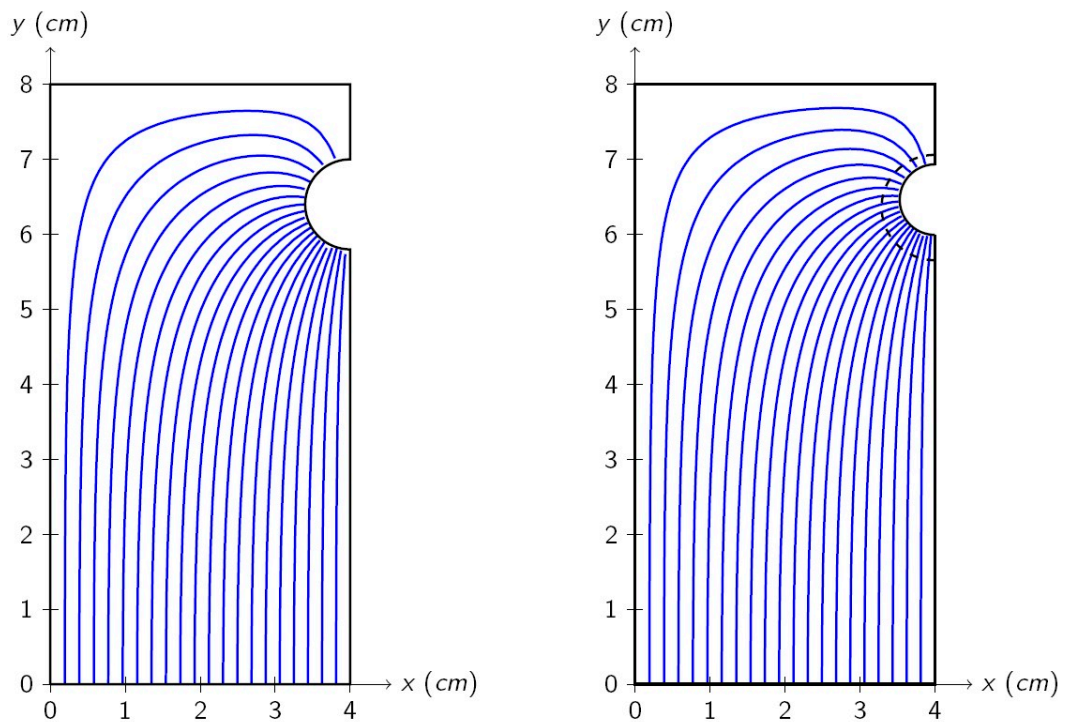


**Figure 3.** Current streamlines (20 of them are shown) initially (left) and after one year of corrosion (right). Dashed line shows the oxide layer.

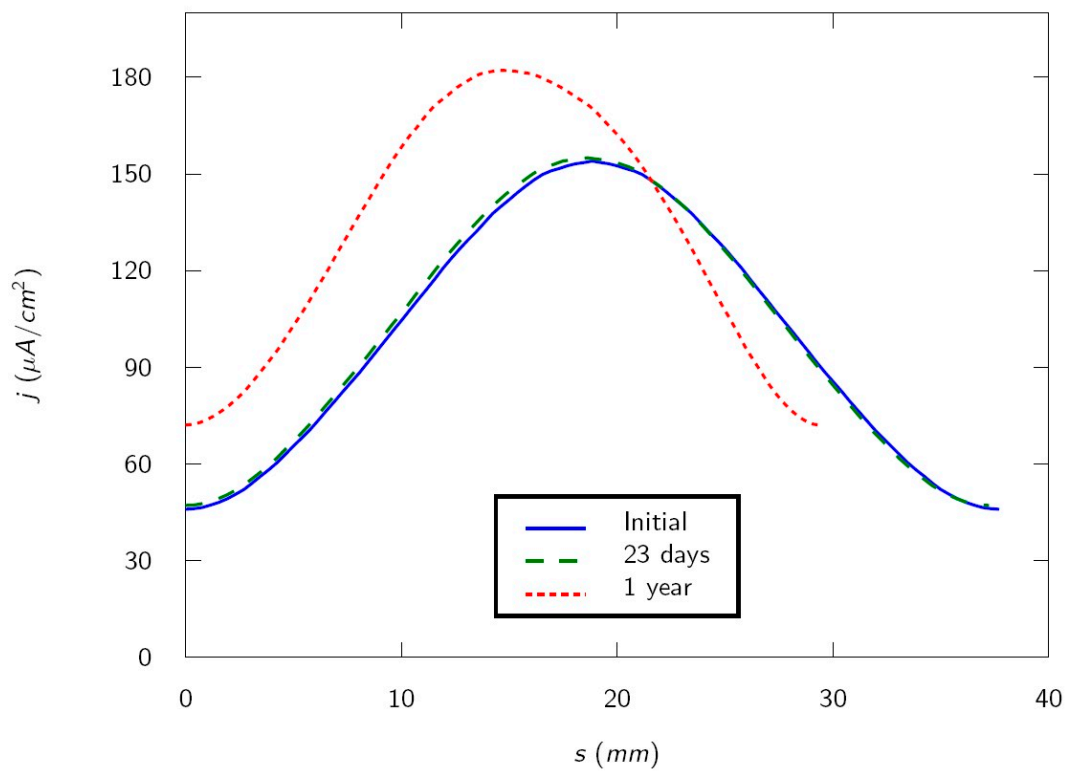


**Figure 4.** Current density on the perimeter of the rebar at several corrosion times.

The difference of radii with respect to the initial radius of the rebar for the metal ( $\Delta r_m = r_m - \frac{D}{2}$ ) and for the oxide ( $\Delta r_{ox} = r_{ox} - \frac{D}{2}$ ) are shown in Figure 5 for four days (appearance of the first cracks on the sample surface) and 23 days (test duration). The values for  $\theta = 0^\circ$  (rebar top, minimum radius difference) and for  $\theta = 180^\circ$  (rebar bottom, maximum radius difference) for several times are listed in Table 3. In this case, it can be seen that, according to the simulation, the first cracks on the sample surface appear with a decrease of rebar radius about 20  $\mu\text{m}$  on the bottom side of the bar, but only about 6  $\mu\text{m}$  on the side toward the cracked mortar surface. This estimation is in good agreement with results of experimental works, which concluded that only a few micrometers of loss in rebar radius are needed to induce visible concrete cover cracks, in experimental conditions similar to those modeled in this case [9].

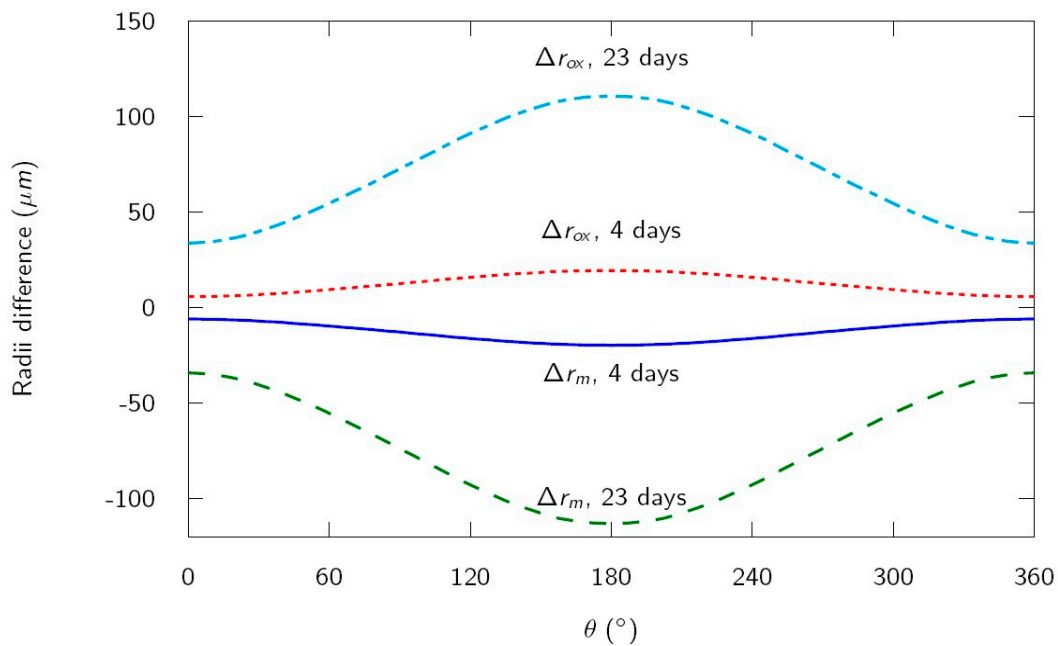


Figure 5. Difference of calculated radii of the rebar after four days and 23 days of corrosion.

Table 3. Difference of radii for the metal and for the layer of oxides calculated at several corrosion times.

	$\Delta r_m$ ( $\mu\text{m}$ )		$\Delta r_{ox}$ ( $\mu\text{m}$ )	
	Top	Bottom	Top	Bottom
4 days	-	-19.6	5.9	19.6
23 days	-34.7	-113.2	33.9	111.1
1 year	-666.9	-1932.1	599.8	1446.6

Graph of  $\Delta r_{ox}$  in Figure 5 resembles a sinusoidal function of the form (12).

$$\Delta r_{ox} = a + b \cos \theta \tag{12}$$

Figure 6 shows a linear fit of  $\Delta r_{ox}$  versus  $\cos \theta$  for four days (when the first cracks appear) and 23 days (test duration). A good fit is obtained ( $r = 0.9998$  in both cases). Fitting goodness decreases for longer times ( $r = 0.9962$  for 1 year). Therefore, it can be stated that an increase of the rebar diameter depends on angle  $\theta$  in approximately a sinusoidal way for not long times. A cracking model with a radius dependence of the corroded bar linear with a vertical coordinate has been proposed [13]. It is worth noting that the proposed dependence (12) with  $\theta$  is equivalent to the dependence used in Reference [13], and, thus, the presented electrochemical model supports the use of this dependence in the cracking model.



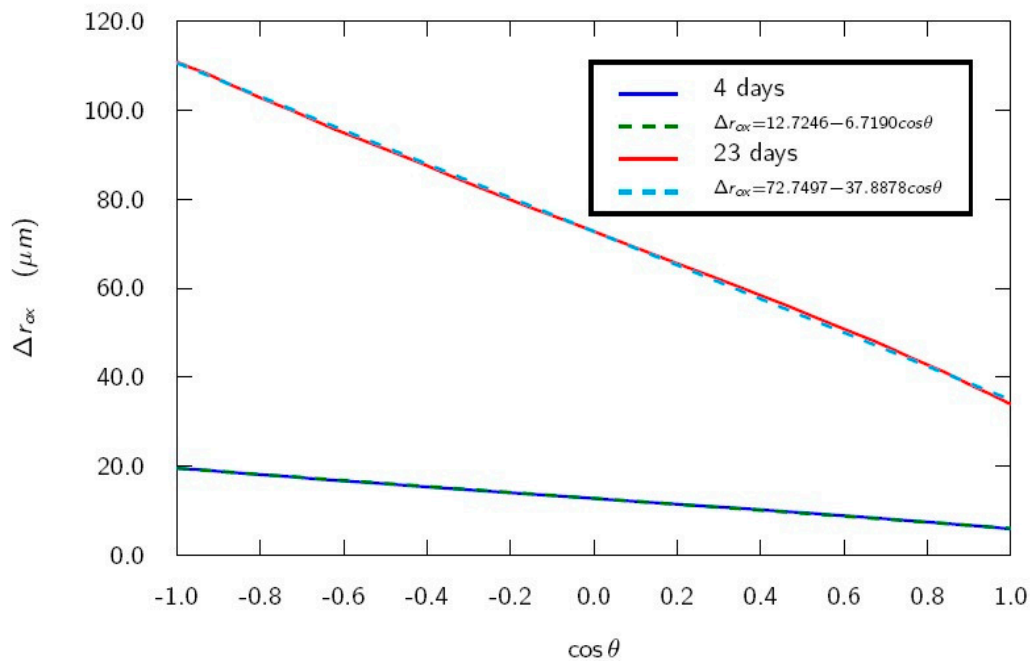


**Figure 6.** Difference of oxide radius with respect to the initial radius versus  $\cos \theta$  after four days and 23 days of corrosion.

## 5. Conclusions

The following conclusions can be drawn from the electrochemical model proposed in this paper.

1. Rebar-shape time-evolution during a forced corrosion test can be estimated.
2. The side of the rebar nearest to the cathode is the most affected by corrosion, suffering the highest current density, highest metal radius reduction, and highest volume increase due to corrosion product creation.
3. When the first cracks appear, the rebar radius increases on the side nearest the mortar surface, which is about 6 m.
4. Dependence of the expanded rebar radius along the rebar perimeter is approximately sinusoidal with a perimeter angle if corrosion time is not very long.
5. The estimated rebar shape time-evolution could be used as input for a mechanical mortar cracking model in order to estimate crack evolution during the forced corrosion test.

**Author Contributions:** Conceptualization, G.d.V. and M.A.C. Methodology, P.P., M.M., and G.d.V. Software, G.d.V. and E.G.S. Validation, P.P. and M.M. Formal Analysis, E.G.S. and P.P. Investigation, M.M. and E.G.S. Resources, P.P. and E.G.S. Data Curation, P.P. and M.M. Writing—Original Draft Preparation, G.d.V. and E.G.S. Writing—Review and Editing, M.A.C. Visualization, G.d.V. and M.M. Supervision, M.A.C. Project Administration, M.A.C. Funding Acquisition, M.A.C.

**Funding:** We thank the funding received for this research from the Spanish Agencia Estatal de Investigación (AEI) and Fondo Europeo de Desarrollo Regional (FEDER) through project BIA2016-80982-R. One of us (M. Miró) acknowledges a pre-doctoral fellowship from the Spanish Ministerio de Educación (FPU16/04078).

**Acknowledgments:** We are grateful to Lafarge-Holcim Spain for providing the cement samples for preparing the reinforced mortar specimens. Thanks are also due to Jaime Ramis and Jesús Carbajo, from the University of Alicante for fruitful discussions.

**Conflicts of Interest:** The authors declare no conflict of interest.

## References

1. ACI Committee 222R-96. *Corrosion of Metals in Concrete*; American Concrete Institute (ACI): Farmington Hills, MI, USA, 1996.
2. Suda, K.; Misra, S.; Motohashi, K. Corrosion products of reinforcing bars embedded in concrete. *Corros. Sci.* **1993**, *35*, 1543–1549. [[CrossRef](#)]
3. Alonso, C.; Andrade, C.; Rodríguez, J.; Díez, J.M. Factors controlling cracking of concrete affected by reinforcement corrosion. *Mater. Struct.* **1998**, *31*, 435–441. [[CrossRef](#)]
4. Weyers, R.E.; Liu, Y. Modeling the time-to-corrosion cracking in chloride contaminated reinforced concrete structures. *ACI Mater. J.* **1998**, *95*, 675–681.
5. Bertolini, L.; Elsener, B.; Pedersen, P.; Polder, R. *Corrosion of Steel in Concrete*; Wiley-VCH: Weinheim, Germany, 2004.
6. Uomoto, T.; Misra, S. Behaviour of concrete beams and columns in marine environment when corrosion of reinforcing bars takes place. In *2nd International Conference on Concrete in Marine Environment*; ACI SP-109; American Concrete Institute (ACI): Farmington Hills, MI, USA, 1988; pp. 127–146.
7. Ministerio de Fomento. *EHE-08, Instrucción de Hormigón Estructural (EHE-08, Spanish Structural Concrete Code)*; Ministerio de Fomento: Madrid, Spain, 2010. (In Spanish)
8. Jamali, A.; Angst, U.; Adey, B.; Elsener, B. Modeling of corrosion-induced concrete cover cracking: A critical analysis. *Constr. Build. Mater.* **2013**, *42*, 225–237. [[CrossRef](#)]
9. Andrade, C.; Alonso, C.; Molina, F.J. Cover cracking as function of bar corrosion: Part 1—Experimental test. *Mater. Struct.* **1993**, *26*, 453–464. [[CrossRef](#)]
10. Muthulingam, S.; Rao, B.N. Non-uniform corrosion states of rebar in concrete under chloride environment. *Corros. Sci.* **2015**, *93*, 267–282. [[CrossRef](#)]
11. Cheng, X.; Su, Q.; Ma, F.; Liu, X.; Liang, X. Investigation on crack propagation of concrete cover induced by non-uniform corrosion of multiple rebars. *Eng. Fract. Mech.* **2018**, *201*, 366–384. [[CrossRef](#)]
12. Qiao, D.; Nakamura, H.; Yamamoto, Y.; Miura, T. Crack patterns of concrete with a single rebar subjected to non-uniform and localized corrosion. *Constr. Build. Mater.* **2016**, *116*, 366–377. [[CrossRef](#)]
13. Guzmán, S.; Gálvez, J.C. Modelling of concrete cover cracking due to non-uniform corrosion of reinforcing steel. *Constr. Build. Mater.* **2017**, *155*, 1063–1071. [[CrossRef](#)]
14. Su, R.K.L.; Zhang, Y. A novel elastic-body-rotation model for concrete cover spalling caused by non-uniform corrosion of reinforcement. *Constr. Build. Mater.* **2019**, *213*, 549–560. [[CrossRef](#)]
15. Zhang, Y.; Su, R.K.L. Concrete cover delamination model for non-uniform corrosion of reinforcements. *Constr. Build. Mater.* **2019**, *223*, 329–340. [[CrossRef](#)]
16. Jin, L.; Zhang, R.; Du, X.; Li, Y. Investigation on the cracking behavior of concrete cover induced by corner located rebar corrosion. *Eng. Fail. Anal.* **2015**, *52*, 129–143. [[CrossRef](#)]
17. Sola, E.; Özbolt, J.; Balabanić, G.; Mir, Z.M. Experimental and numerical study of accelerated corrosion of steel reinforcement in concrete: Transport of corrosion products. *Cem. Concr. Res.* **2019**, *120*, 119–131. [[CrossRef](#)]
18. Idrissi, H.; Limam, A. Study and characterization by acoustic emission and electrochemical measurements of concrete deterioration caused by reinforcement steel corrosion. *NDTE Int.* **2003**, *36*, 563–569. [[CrossRef](#)]
19. Ye, H.; Jin, N.; Fu, C.; Jin, X. Rust distribution and corrosion-induced cracking patterns of corner located rebar in concrete cover. *Constr. Build. Mater.* **2017**, *156*, 684–691. [[CrossRef](#)]
20. Dong, B.; Shi, G.; Dong, P.; Ding, W.; Teng, X.; Qin, S.; Liu, Y.; Xing, F.; Hong, S. Visualized tracing of rebar corrosion evolution in concrete with x-ray microcomputed tomography method. *Cem. Concr. Compos.* **2018**, *92*, 102–109. [[CrossRef](#)]
21. Zhang, J.; Ling, X.; Guan, Z. Finite element modeling of concrete cover crack propagation due to non-uniform corrosion of reinforcement. *Constr. Build. Mater.* **2017**, *132*, 487–499. [[CrossRef](#)]
22. Chernin, L.; Val, D.V.; Volokh, K.Y. Analytical modelling of concrete cover cracking caused by corrosion of reinforcement. *Mater. Struct.* **2010**, *43*, 543–556. [[CrossRef](#)]
23. Guzmán, S.; Gálvez, J.C.; Sancho, J.M. Cover cracking of reinforced concrete due to rebar corrosion induced by chloride penetration. *Cem. Concr. Res.* **2011**, *41*, 893–902. [[CrossRef](#)]

24. Climent, M.A.; de Vera, G.; Viqueira, E.; López, M.M. Generalization of the possibility of eliminating the filtration step in the determination of acid-soluble chloride content in cement and concrete by potentiometric titration. *Cem. Concr. Res.* **2004**, *34*, 2291–2295. [[CrossRef](#)]
25. UNE-EN 197-1 (2011). “Cemento. Parte 1: Composición, Especificaciones y Criterios de Conformidad de los Cementos Comunes” (“Cement. Part 1: Composition, Specifications and Conformity Criteria for Common Cements”); Equivalent to the European Standard EN 197-1; Asociación Española de Normalización y Certificación: Madrid, Spain, 2000. (In Spanish)
26. ASTM G 1-90—*Standard Practice for Preparing, Cleaning and Evaluating Corrosion Test Specimens*; American Society for Testing and Materials (ASTM): West Conshohocken, PA, USA, 1990.
27. Climent, M.A.; Miró, M.; Carbajo, J.; Poveda, P.; de Vera, G.; Ramis, J. Use of non-linear ultrasonic techniques to detect cracks due to steel corrosion in reinforced concrete structure. *Materials* **2019**, *12*, 819. [[CrossRef](#)]
28. Molina, F.J.; Alonso, C.; Andrade, C. Cover cracking as function of rebar corrosion: Part 2—Numerical model. *Mater. Struct.* **1993**, *26*, 532–548. [[CrossRef](#)]
29. Carey, G.F.; Oden, J.T. *Finite elements. Vol VI, Fluid Mechanics*; Prentice-Hall: Upper Saddle River, NJ, USA, 1986.
30. Zienkiewicz, O.C.; Taylor, R.L. *The Finite Element Method. Vol. 1: The Basis*; Butterworth-Heinemann: Oxford, UK, 2000.
31. Matlab. Available online: <http://www.mathworks.com/help/matlab/index.html> (accessed on 20 June 2019).
32. Matlab Online Documentation for Delaunay. Available online: [https://es.mathworks.com/help/matlab/ref/delaunay.html?s\\_tid=gn\\_loc\\_drop](https://es.mathworks.com/help/matlab/ref/delaunay.html?s_tid=gn_loc_drop) (accessed on 20 June 2019).
33. *Handbook of Chemistry and Physics*, 66th ed.; West, R.C., Ed.; CRC Press: Boca Raton, FL, USA, 1985.



© 2019 by the authors. Licensee MDPI, Basel, Switzerland. This article is an open access article distributed under the terms and conditions of the Creative Commons Attribution (CC BY) license (<http://creativecommons.org/licenses/by/4.0/>).